Research Article Vol. 3, No. 11 / November 2016 / Optica 1171

optica

High-Q silicon nitride microresonators exhibiting low-power frequency comb initiation

Yi Xuan,[1,†] Yang Liu,[1,†] Leo T. Varghese,[1] Andrew J. Metcalf,[1] Xiaoxiao Xue,[1] Pei-Hsun Wang,[1] Kyunghun Han,[1] Jose A. Jaramillo-Villegas,[1,2] Abdullah Al Noman,[1] Cong Wang,[1] Sangsik Kim,[1] Min Teng,[1] Yun Jo Lee,[1] Ben Niu,[1] Li Fan,[1] Jian Wang,[1] Daniel E. Leaird,[1] Andrew M. Weiner,[1] and Minghao Qi[1,*]

[1]School of Electrical and Computer Engineering and the Birck Nanotechnology Center, Purdue University, West Lafayette, Indiana 47907, USA
[2]Facultad de Ingenierías, Universidad Tecnológica de Pereira, Pereira, RIS 660003, Colombia
*Corresponding author: mqi@purdue.edu

Received 17 February 2016; revised 17 July 2016; accepted 27 July 2016 (Doc. ID 259421); published 24 October 2016

Optical resonators with high quality factors (*Q*s) are promising for a variety of applications due to the enhanced nonlinearity and increased photonic density of states at resonances. In particular, frequency combs (FCs) can be generated through four-wave mixing in high-*Q* microresonators made from Kerr nonlinear materials such as silica, silicon nitride, magnesium fluoride, and calcium fluoride. These devices have potential for on-chip frequency metrology and high-resolution spectroscopy, high-bandwidth radiofrequency information processing, and high-data-rate telecommunications. Silicon nitride microresonators are attractive due to their compatibility with integrated circuit manufacturing; they can be cladded with silica for long-term stable yet tunable operation, and allow multiple resonators to be coupled together to achieve novel functionalities. Despite previous demonstrations of high-*Q* silicon nitride resonators, FC generation using silicon nitride microresonator chips still requires pump power significantly higher than those in whispering gallery mode resonators made from silica, magnesium, and calcium fluorides, which all have shown resonator *Q*s between 0.1 and 100 billion. Here, we report on a fabrication procedure that leads to the demonstration of "finger-shaped" Si_3N_4 microresonators with intrinsic *Q*s up to 17 million at a free spectrum range (FSR) of 24.7 GHz that are suitable for telecommunication and microwave photonics applications. The frequency comb onset power can be as low as 2.36 mW and broad, single FSR combs can be generated at a low pump power of 24 mW, both within reach of on-chip semiconductor lasers. Our demonstration is an important step toward a fully integrated on-chip FC source. © 2016 Optical Society of America

OCIS codes: (230.5750) Resonators; (220.4000) Microstructure fabrication; (190.4360) Nonlinear optics, devices.

http://dx.doi.org/10.1364/OPTICA.3.001171

1. INTRODUCTION

Optical resonators with high quality factors (*Q*s) can strongly enhance optical nonlinearity, increase the density of states of resonant optical modes, and achieve long photon life time [1]. When such resonators are integrated with other photonic and electronic devices on a silicon (Si) chip or a multichip assembly to achieve stable and tunable operation, they can bring a large range of applications onto chips, including linear and nonlinear optical information processing [2,3], spectroscopic sensing [4,5], quantum entanglement of radiation and matter [6,7], cavity optomechanics [8], and frequency comb (FC) generation [9,10]. In particular, FC generation in high-*Q* microresonators has attracted intense attention with target applications ranging from optical clocks and frequency metrology [11] to more novel techniques in high-speed telecommunication [12] and RF photonics [13].

Chip-scale FCs, or microcombs, can have characteristics inherent in traditional mode-locked laser-based combs such as low noise and high stability [11], together with the benefit of a reduced footprint and potential for more functionalities and low-cost manufacturing. An additional draw to the microcomb platform is the possibility of generating FCs with repetition rates spanning from 10 to 100 s of GHz—a regime which has remained a challenge for traditional mode-locked laser techniques due to long laser cavity lengths.

Kerr comb generation in microresonators starts when an external continuous-wave (CW) laser is tuned into a cavity resonance; this causes intracavity power to build, which enables additional cavity modes to oscillate through nonlinear wave mixing [10]. FC formation has now been demonstrated in a variety of Kerr nonlinear materials such as silica [9,14–18], silicon nitride (Si_3N_4) [19–21], aluminum nitride [22], CaF_2 [23], and MgF_2 [24]. Recently, dissipative Kerr solitons have also been demonstrated in MgF_2 and Si_3N_4 optical microresonators [25,26]. Out of these materials, stoichiometric Si_3N_4 has distinctive

advantages. It is compatible with CMOS technology in materials and processing, thus allowing electro-optic integration with the existing Si photonics platform. In addition, Si_3N_4 resonators can be cladded with SiO_2 for long-term operation, offer stable and tunable coupling between the resonator and bus waveguide without mechanical instability, and allow for fabrication of advanced features such as drop ports, heaters, and multiple coupled resonators [27–30].

The major drawback of Si_3N_4-resonator-based FC generation is the high pump power required, typically in tens to hundreds of milliwatts (mWs), which often exceeds the maximum available power from current on-chip tunable laser sources. The threshold pump power P_{th}, according to Ref. [31], can be expressed as

$$P_{\mathrm{th}} = \frac{(1 + (Q_{\mathrm{int}}/Q_{\mathrm{ext}}))^3}{(Q_{\mathrm{int}}/Q_{\mathrm{ext}})} \frac{\pi^2}{2} \frac{n_0^2 R_{\mathrm{eff}} A_{\mathrm{eff}}}{n_2 \lambda Q_{\mathrm{int}}^2}, \quad (1)$$

where Q_{int} and Q_{ext} are the intrinsic and external (or coupling) quality factors, n_o is the material refractive index, n_2 is the Kerr nonlinear coefficient, λ is the pump wavelength in vacuum, and R_{eff} and A_{eff} are the effective radius of the resonator and effective area of the pump mode, respectively. According to Eq. (1), P_{th} will increase linearly with R_{eff}, or resonator size, and pump powers at a few-watt level are common for large resonators to achieve coherent FCs with repetition rate in the tens of GHz range that are most relevant for applications in RF systems and lightwave communications [32,33]. Unfortunately, the advantage of optical integration for Si_3N_4 resonators will not be realized without first demonstrating FC generation at pump power range attainable with on-chip tunable laser sources, i.e., 10–100 mW.

On the other hand, Eq. (1) suggests that the pump power threshold decreases quadratically with increasing quality factor (Q) of the resonator [31], and there has been an elevated focus on optimization of the device fabrication process in order to increase the Q of the integrated resonators [14,33–36]. While high intrinsic Qs up to ~20 million have been reported for large-diameter disk-like Si_3N_4 ring resonators (8 μm wide ring width) [35] and up to 7 million has been reported for few-mode 910 nm thick Si_3N_4 rings [34], to our knowledge no FC has been reported for those high-Q resonators in Si_3N_4 [34–36]. In general, FC generation with Si_3N_4 resonators has not been reported to have threshold pump power comparable to silica ridge disks [15], or CaF_2 [23] and MgF_2 [24] resonators.

In this paper, we demonstrate an intrinsic Q of 17 million in a 600 nm thick, 25 GHz FSR Si_3N_4 "finger-shaped" resonator with comb initiation/threshold power as low as 2.36 mW and single-FSR comb at 24 mW pump power. These numbers are comparable with previous demonstrations of low-threshold-power comb generation with a ridge-shaped SiO_2 resonator having a Q of 2.7×10^8 at 33 GHz FSR (2 mW threshold, see Fig. 1(b) in Ref. [15]), or a 13.81 GHz FSR comb generated with a CaF_2 resonator having a Q as high as 6×10^9 (20–25 mW pump power level, see [23]).

2. DEVICE FABRICATION

This section presents, in reasonable detail, the process steps and variations we have attempted in achieving high-Q Si_3N_4 resonators.

The first step is to achieve crack-free thick stoichiometric Si_3N_4 films of 580–800 nm thickness that have the desired dispersion properties for FC generation [19]. Nam *et al.* [37] proposed to use ring-shaped trenches to prevent film cracking, which typically starts from the edge of the substrate and propagates into the device area. This method has been adopted by Luke *et al.* to achieve a crack-free film of 910 nm in thickness [34]. In Ref. [37] it was pointed out that a staircase etching profile is needed to stop the cracking, and Ref. [34] used a diamond scribe to simulate the staircase etching. Our experience, on the other hand, suggests that if the etching is deep enough, e.g., ~120 μm in depth, a crack-free device region can be achieved without resorting to staircase-shaped etching. Our chips typically occupy an area of 2.5 cm × 1 cm and are surrounded by five trenches, each ~10 μm wide and ~120 μm deep. Figure 1 shows the process schematic of the trench formation. An optical mask defines the islands and trenches in a thick resist (6 μm thick AZ-9260). The wafer was etched in a Deep RIE tool (STS ASE) to form the 120 μm deep trenches. A 3.5 μm thick SiO_2 was then grown in a wet oxidation environment as lower cladding. Stoichiometric Si_3N_4 films have been grown in low-pressure chemical vapor deposition (LPCVD) tools in two locations. Thick films were achieved in multiple installments of 250–300 nm for each deposition. While the deposition tubes were allowed to cool down, no annealing of films was performed between depositions as reported in Ref. [38].

Si_3N_4 films were grown on both patterned 4 inch wafers and cleaved wafer pieces in a ProTemp LPCVD furnace at Purdue's Birck Nanotechnology Center with ammonia (NH_3) and dichlorosilane [$(CH_3)_2SiCl_2$], at a gas flow ratio around 5∶1. At 800°C, the growth rate is around 3 nm/min. We have observed intrinsic Qs up to 1.1×10^7 in a microring that has a radius of 100 μm and waveguide cross section of 0.6 μm × 5 μm.

Several batches of films were also grown on patterned 4 inch wafers in a CMOS foundry (Noel Technologies, Campbell, CA) at 750°C using a proprietary recipe [Fig. 1(b)]. Intrinsic Qs up to 1.7×10^7 were observed with a resonator waveguide cross-section of 0.6 μm × 3 μm (Fig. 5).

After Si_3N_4 deposition, we were able to manually cleave the wafers into 2.5 cm × 1 cm pieces without incurring cracks into the islands. However, we recommend processing the wafers in full without cleaving to improve the uniformity in subsequent film deposition and annealing.

Hydrogen-silsesquioxane (HSQ), an inorganic, negative-tone resist for electro-beam lithography (EBL), was adopted for its high resolution and ability to form a thick film. 1 μm thick HSQ films (FOx −16 from Dow Corning) were patterned with two different EBL systems, both from Raith America, Inc; one is the VB6-UHR-EWF and the other is the EBPG 5200. In the

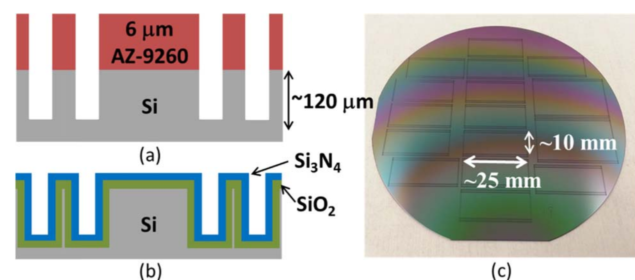

Fig. 1. (a), (b) Process schematic for the deep trench formation. (c) Optical image of a 4" wafer with 600 nm thick Si_3N_4 film grown in a CMOS foundry.

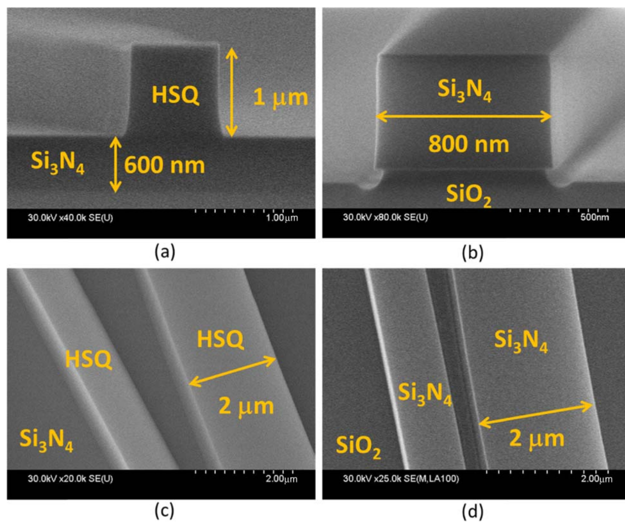

Fig. 2. Scanning electron micrographs showing (a), (b) cross-sectional views of 1 µm thick HSQ on top of 600 nm Si_3N_4 after EBL exposure and 800 nm wide Si_3N_4 waveguide with almost vertical sidewalls; (c), (d) tilted top views of exposed HSQ on Si_3N_4 and etched Si_3N_4 waveguides showing negligible edge and sidewall roughness.

VB6, a field size of 1.3 mm, beam current of 4 nA, and beam step size of 5 nm were chosen to deliver a dose ~2500 $\mu C/cm^2$. In EBPG 5200, a field size of 0.5 mm, beam current of 1 nA, and beam step size of 2 nm were adopted to deliver similar doses to the HSQ films. Figures 2(a) and 2(c) are scanning electron microscope (SEM) micrographs showing the vertical and smooth sidewalls of EBPG 5200 exposed thick HSQ films, which we believe will benefit the subsequent etching process.

After the exposure and development, Si_3N_4 was dry-etched with CHF_3/O_2-based chemistry in an inductively coupled, high-density plasma etching tool (Panasonic P610). The etching selectivity between exposed HSQ (effectively SiO_2) and Si_3N_4 is close to 3. The vertical sidewall of thick HSQ film, as well as the high etching selectivity, allowed us to achieve near-vertical sidewalls for our Si_3N_4 resonators [Fig. 2(b)] without visible sidewall roughness [Fig. 2(d)]. This sets us apart from previously reported resonators, which typically have slanted sidewalls due to using organic resists such as ZEP 520 [35] and reflowed MaN-26 [34]. The thick Si_3N_4 film that was also deposited on the back of the wafer during LPCVD was subsequently dry-etched away to eliminate the stress on the substrate.

An upper cladding of 3 µm low-temperature oxide (LTO) was then deposited using LPCVD. We note that there were air voids in narrow gaps (below 1 : 1 width-to-height aspect ratio) between the bus waveguide and the resonator (Fig. 3). This void is expected to cause excess loss at the coupling region [39]. In this report, no effort is attempted to quantify such excess coupling loss and it will be treated as part of the roundtrip loss; thus, the extracted intrinsic quality factors (Q_{int}) will be underestimated [36].

At this stage, several devices were manually cleaved from the wafer for testing, and we observed intrinsic Qs of resonators as high as 2.7×10^6 for a ring with a 300 µm radius and a waveguide cross section of 0.3 µm × 3 µm. As Si_3N_4 films with thickness <0.3 µm are routinely used in CMOS manufacturing as an etch mask or etch stop, and all the processes so far are CMOS compatible, e.g., no high-temperature annealing, this result suggests that low-loss waveguides and high-Q resonators from Si_3N_4 might be available for silicon photonics using standard front-end-of-line CMOS processes.

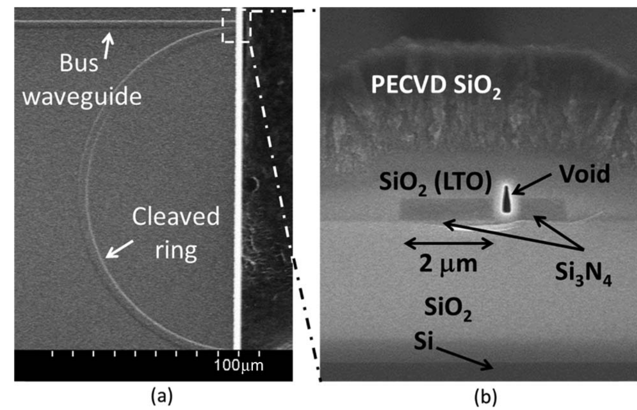

Fig. 3. SEM micrographs showing (a) the cleaved ring and (b) the void in the gap region between the bus waveguide and ring waveguide.

To improve the Qs, we follow the procedure in Ref. [34] and performed high-temperature annealing at 1150°C–1200°C for 3 h to remove the residue N H bonds in the SiN film and densify the LTO upper cladding. We have observed increase of intrinsic Qs by roughly an order of magnitude. We also attempted annealing at higher temperature, up to 1350°C above which the Si substrate is melted in a ceramic furnace, but did not observe further improvement in intrinsic Qs. The coupling between the bus waveguides and rings in certain devices had increased, suggesting the collapse of voids in the gap region even though no visual evidence has been obtained.

We have also investigated the effect of upper cladding on the intrinsic quality factors. A set of devices went through the annealing process without upper cladding deposition, and we have observed intrinsic Qs up to 4.7×10^6.

To minimize the mechanical vibration of the optical fibers during measurement with high input powers necessary for FC generation, U-shaped grooves were dry-etched into the Si substrate using a deep RIE etching tool (STS-ASE). Those U-grooves accommodate the lensed fibers and allow them to be placed close to the waveguide edges (Fig. 4). Compared to previous practice of using V-shaped grooves, our U-grooves can be readily fabricated in a CMOS foundry and do not depend on the crystal orientation of the substrate. Moreover, it does not create any large undercut which would effectively suspend, e.g., without substrate support, the waveguides at the edges of the chips.

The fabricated devices are stable in laboratory environment and there is no noticeable performance degradation after accumulation of particles and liquid stains, or going through standard solvent cleaning, i.e., rinse in acetone, methanol, and isopropanol.

Table 1 summarizes the various process variations and the corresponding highest observed intrinsic Qs. All films were deposited in the foundry unless explicitly stated otherwise. Note, however, the observed Qs by no means suggest any upper limits for the processes, and additional process optimizations are ongoing.

3. OPTICAL MEASUREMENTS

Figure 5(a) shows an optical image of the fabricated Si_3N_4 microresonator with a waveguide cross section of 3 µm × 600 nm. The

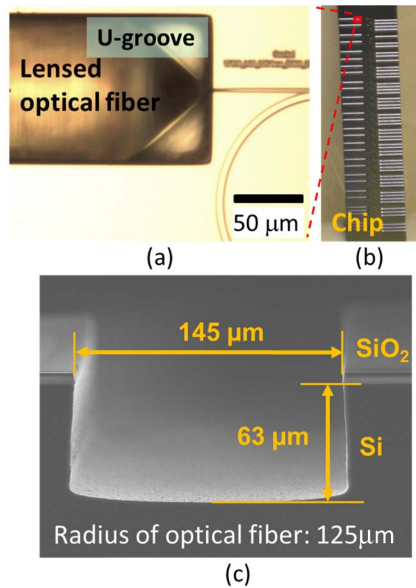

Fig. 4. Images of the U-shaped grooves that house the lensed fiber tips.

total length of the SiN resonator is 5920 μm, which corresponds to an effective radius of 950 μm and a free spectral range (FSR) of ~25 GHz. The total fiber-to-fiber coupling loss is measured to be ~5 dB. Since the propagation loss of the Si_3N_4 waveguide is usually small (<0.01 dB/mm) and the bus waveguide in this work is very short (~1 mm), as seen in Fig. 5(a), the propagation loss in the bus waveguide is negligible compared to edge coupling losses. Hence, the coupling loss at each facet is estimated to be ~2.5 dB.

We utilized two independent methods to accurately determine the quality factors of the SiN resonators. First, we measured the transmission spectra of the resonances by scanning a single-mode laser at low power through the resonances. To accurately determine the laser wavelength, we used the frequency-comb-assisted spectroscopy method [40], in which the laser frequency sweep is determined by beating with a self-referenced fiber comb (Menlo Systems). We then independently verify the Qs using a cavity ring-down measurement [41].

Our systematic characterization starts with the determination of the polarization of the modes. The relatively vertical sidewalls allow us to categorize the modes into quasi-transverse electric (TE) and quasi-transverse magnetic (TM) modes. The input light from a tunable laser light source (New Focus TLB-6728-LN) is transmitted through a fiber polarization controller before coupling into the inverse nanotaper of the device through a lensed fiber inserted into a U-groove [Fig. 4(a)]. A small adjustment of the fiber tip position helps achieve maximum power coupling. On the output side, we first use a collimating lens and a linear polarizer to determine the polarization of the light emanating from the output facet [another inverse taper connected to a U-groove, see Fig. 4(b)]. We then adjust the fiber polarization controller to achieve quasi-TE or quasi-TM output by adjusting the fiber polarization controller at the input side.

Once the polarization of the output light is set, we insert another lensed fiber to the output U-groove to characterize the fiber-to-fiber insertion loss. We found that the quasi-TE modes generally have about 1–2 dB lower insertion loss than that of the quasi-TM modes, and have utilized this property to tune the input polarization controller and set the polarization of the incoming light roughly to TE, bypassing the collimator and linear polarizer setup. Once a resonance dip is identified in a scanned spectrum, the input light wavelength is tuned to the dip of the resonance and the polarization is further adjusted to maximize the attenuation. In the case of Fig. 5(c), 17 dB of attenuation was achieved, which suggested very high purity of TE polarization (<2% composition of TM polarization).

We rarely observe resonance splitting in the high-Q modes, suggesting the lack of structural defects [42,43] that could excite backward propagating modes. This is another indication of the high fabrication quality.

A normalized section of the measured transmission spectrum for the quasi-TE modes is shown in Fig. 6(a) for wavelengths between 1554 and 1557 nm. There are three modes within every ~0.2 nm wavelength range, corresponding to an FSR of ~25 GHz. Different modes possess different FSRs, extinction ratios, and intrinsic quality factors, but only one mode achieves high intrinsic Qs over 10^7 [Fig. 6(b)]. The existence of high Qs in multiple resonance wavelengths instead of one or a few is a strong indication that the high Qs are due to the low propagation loss inside the resonator rather than unusual mode interactions or irregularities during wavelength scanning.

To determine the actual mode that exhibits high Qs, we simulated the effective indices of three quasi-TE modes (TE_{00}, TE_{01}, and TE_{02}). The material index dispersion of the deposited Si_3N_4 film was measured with a spectroscopic ellipsometer (J. A. Wollan). Group index, n_g, is then calculated for a straight Si_3N_4 waveguide with a cross section of 600 nm × 3 μm and a sidewall angle of 84°. The FSR is then calculated using $\text{FSR} = c/Ln_g$, where L is the perimeter of the resonator calculated with the resonator layout and c is the speed of the light. We note that the resonator contains several bends, and the modes will be slightly pushed to the outer edge. However, from Fig. 5(a), the resonator is mainly comprised of straight waveguides and the deviation caused by our approximation is expected to be low.

Table 1. Process Variations and the Highest Observed Intrinsic *Q*s

Process Variations	Highest Intrinsic Q	Resonator Waveguide Cross Section	Resonator Radius [See Fig. 5(a) for Bending and Effective Radii]
"Finger-shaped" racetracks	1.7×10^7	0.6 μm thick, 3 μm wide	100 μm bending, 950 μm effective
Rings	1.3×10^7	0.6 μm thick, 3 μm wide	100 μm
Without upper cladding	4.7×10^6	0.6 μm thick, 3 μm wide	100 μm bending, 400 μm effective
Without annealing	2.7×10^6	0.3 μm thick, 3 μm wide	200 μm
Fabricated on wafer pieces rather than 4" wafers	3.2×10^6	0.75 μm thick, 2 μm wide	200 μm
Films deposited at Purdue	1.1×10^7	0.6 μm thick, 5 μm wide	100 μm

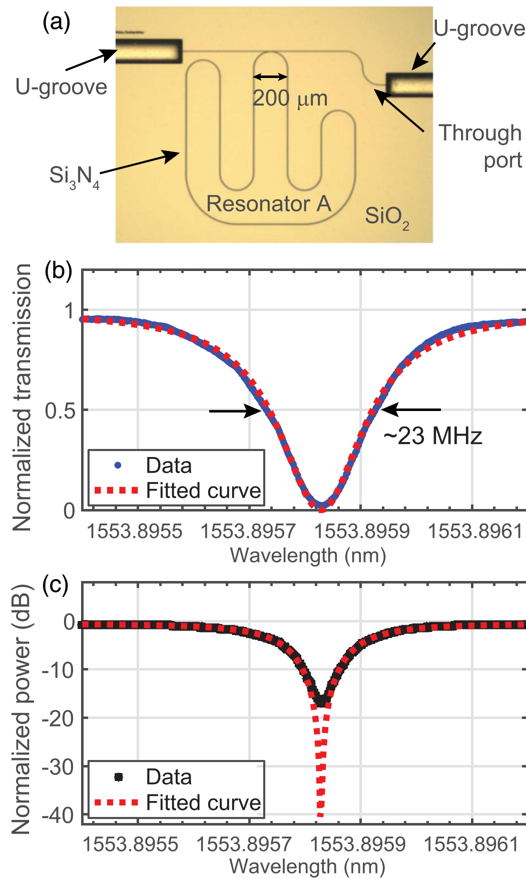

Fig. 5. (a) Optical image showing the "finger-shaped" high-Q resonator with through port only (hereafter referred to as resonator A). The bending radius is set to 100 μm, and the gap between the bus waveguide and the resonator is 200 nm. (b) Normalized transmission spectrum at a resonance showing critical coupling. The Lorentzian fitting yields a loaded Q of 8.33 million and intrinsic Q of 16.6 million. (c) Semi-logarithmic plot of (b) showing a measured on-resonance attenuation of 17 dB and a fitted attenuation over 40 dB.

Table 2 clearly shows a high degree of matching between the measured FSR of the high-Q mode and the calculated FSR of the TE_{00} mode, which is the fundamental TE mode. The FSRs of the other two modes also match well with those of TE_{01} and TE_{02}.

We then calculated loaded quality factors (Q_{loaded}) for the TE_{00} modes of the resonator A [Fig. 5(a)] by fitting a Lorentzian shape of the measured transmission spectrum at each resonance.

High-resolution transmission measurements at three closely spaced resonance dips at 1553.8958, 1556.6858, and 1553.697 nm are shown in Figs. 5(b), 5(c), 7(a), and 7(b), respectively. Note that there was no temperature control for the high-Q device, so the wavelengths at which the resonance dips were observed could be slightly different for multiple measurements at different times.

Table 2. Simulated and Measured Free Spectral Range of Resonator A at ~1554 nm Wavelength

Measured Modes	High-Q mode	Mode 2	Mode 3
Measured FSR	24.7 GHz	24.2 GHz	23.5 GHz
Simulated mode	TE_{00}	TE_{01}	TE_{02}
Calculated FSR	24.7 GHz	24.15 GHz	23.3 GHz

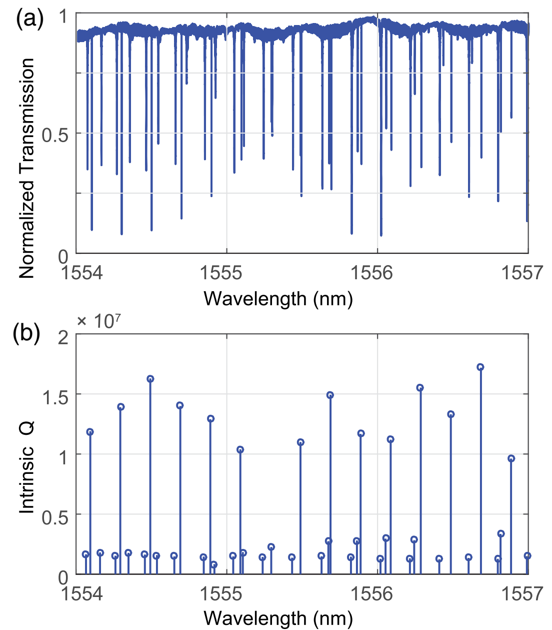

Fig. 6. (a) Normalized transmission spectrum. (b) Extracted intrinsic Qs of three families of modes showing one mode having consistently higher intrinsic Qs than the other two modes. We fitted loaded Qs and assumed under-coupling when calculating the intrinsic Qs from the extinction ratios.

At the resonance near 1553.8958 nm [Figs. 5(b) and 5(c)], we found excellent match between the measured spectrum and Lorentzian fitting except near the minimum transmission, where the fitting predicted over 40 dB attenuation. We achieved 17 dB attenuation and believe it is limited by our manual fiber polarization controller and the voids in the cladding at the coupling region, which may excite high-order modes and/or orthogonal polarizations. For this reason, we argue that the resonance is at critical coupling and determined an intrinsic Q of 16.6 million from a fitted loaded Q of 8.33 million.

For resonances away from critical coupling and if the maximum attenuation can be accurately measured, one can calculate the Q_{int} with

$$Q_{\text{int}} = \frac{2Q_{\text{loaded}}}{(1 \pm \sqrt{T_{\text{min}}})}, \quad (2)$$

where T_{min} refers to the normalized transmission right at the resonance [43]. In the under-coupled regime, Eq. (2) takes the + sign and the over-coupled regime takes the − sign.

Figure 7(a) shows a normalized transmission spectrum at a slightly longer wavelength, and the on-resonance transmission is relatively high at ~0.4. Using a method documented in the supplemental information of [27], we confirmed that the resonance is at the under-coupled regime and fitted a loaded Q of 13.9 million and an intrinsic Q of 17 million. These numbers are also highly consistent with Eq. (2).

Figure 7(b) represents a more complicated case. The resonance is one FSR shorter in wavelength than the resonance at critical coupling [Fig. 5(b)], and has a slightly lower on-resonance attenuation at 15 dB. The fitted curve matches almost exactly with the

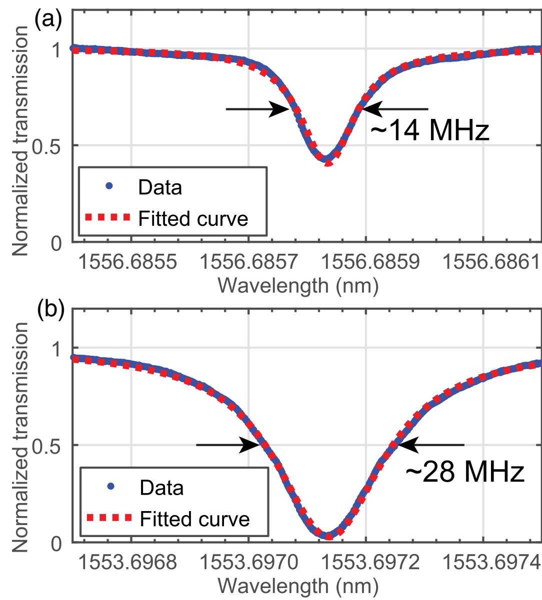

Fig. 7. Normalized transmission spectra and their fitting at two additional resonance dips for resonator A. (a) Resonance showing a fitted loaded Q of 14 million and intrinsic Q of 17 million. (b) Lorentzian fitting at a resonance near critical coupling resulted in a loaded Q of 6.9 million. Assuming slight over-coupling between the bus waveguide and resonator, we fitted an intrinsic Q of 16.8 million, which is consistent with intrinsic Qs shown in (a) and Fig. 5(b).

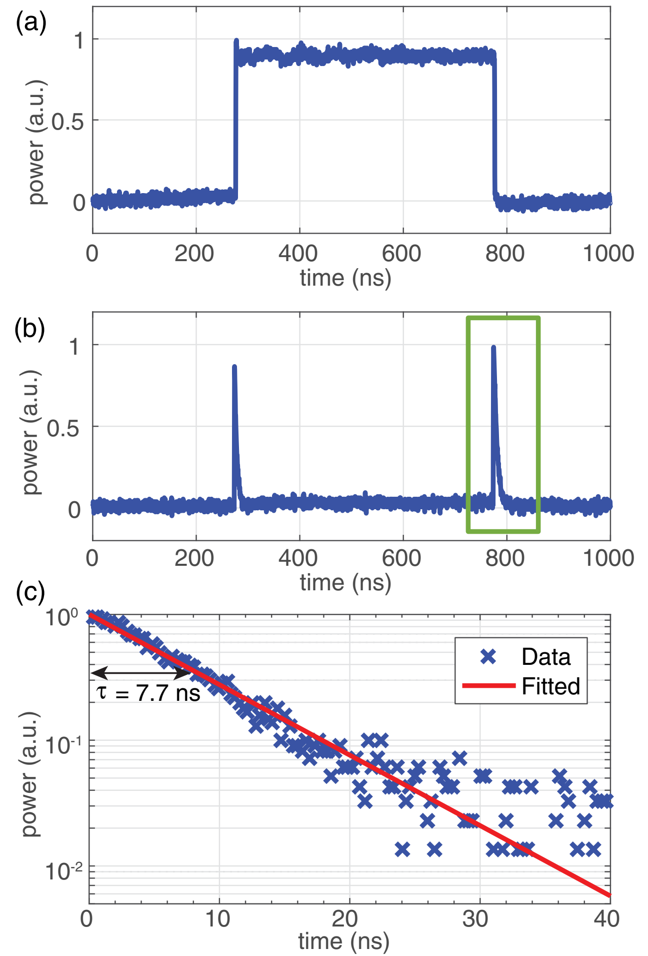

Fig. 8. Cavity ring-down measurement of photon lifetime. (a) Gating signal. (b) Cavity response signal. (c) Semi-log plot of the cavity ring-down signal.

transmission measurement, including the minimum transmission at resonance. Unfortunately, the method in Ref. [27] cannot unequivocally determine the coupling regime when the coupling is very close to critical. With a loaded Q of 6.9 million and a minimum transmission of −15 dB, the intrinsic Q would be 11.8 million assuming under-coupling and 16.8 million assuming over-coupling. Given the very small wavelength difference (~0.199 nm, or 24.7 GHz), it would be reasonable to assume that the intrinsic Q does not change appreciably for the same mode; thus, we conclude it is in the (slightly) over-coupled regime and the intrinsic Q is 16.8 million. This is further corroborated with the matching between the calculated and observed comb generation threshold reported in the next section.

To confirm the loaded Q values just obtained, we performed cavity ring-down measurements [41] to directly measure the photon lifetimes. In order to quickly turn off the pump, we utilized a high-extinction $LiNbO_3$ intensity modulator driven by an electronic arbitrary waveform generator programmed to carve a 1 MHz 50% duty cycle square wave from the CW pump. The average power at the input of resonator was −7 dBm to mitigate the optical nonlinearity. The optical signal at the output of the resonator is coupled via lensed fiber and detected with a 12 GHz photodetector. The electrical signal is then amplified with a low-noise amplifier before being detected on a fast real-time scope (20 Gs/s). Figure 8(a) serves as a reference and shows the optical gating signal when the pump is far detuned from resonance. When tuned into resonance, we observe two peaks [Fig. 8(b)] that temporally coincide with the rising and falling edges of the input optical signal. At the instant the pump is gated on, we observe the first peak, whose amplitude is equivalent to the incident wave. As the field in the resonator begins to charge up, the measured waveform drops to zero due to interference between the incident and out-coupled fields. When the pump is gated off, the incident field becomes zero and we just are left with the decaying out-coupled field from the cavity. Selecting this falling edge and performing a least-squares fit, we calculate a time constant of 6.6 and 7.7 ns for the 1553.697 and 1553.896 resonances, respectfully. In order to help visualize the time constant, we provide a log-plot of the falling edge data along with the least-squares fit in Fig. 8(c) for the resonance at 1553.896 nm. The loaded Q can be directly calculated from the fall time using $Q_{\text{loaded}} = \omega\tau$, where ω is the frequency of the light and τ is the time constant in the cavity ring-down measurements. The intrinsic Q is estimated using the $Q_{\text{int}}/Q_{\text{loaded}}$ ratio calculated from the transmission spectrum.

A summary of the Q measurements from both the transmission and cavity ring-down experiments is presented in Table 3, showing good level of consistency between the two measurements.

The fabrication process allows multiple bus waveguides to be coupled to the high-Q resonator. Figure 9(a) shows a resonator (referred to as resonator B) with both a through port and a drop port. High Qs up to 8.3 million loaded and 11 million intrinsic have been observed. The drop port may allow additional investigation into the microcomb generation—for example, more

Table 3. Summary of Q Values Obtained in Transmission and Cavity Ring-Down Measurements

Resonance Wavelength (nm)	Transmission Loaded	Transmission Intrinsic	Cavity Ring-Down Loaded	Cavity Ring-Down Intrinsic
1553.697	6.93×10^6	1.68×10^7	8.06×10^6	1.95×10^7
1553.896	8.33×10^6	1.66×10^7	9.34×10^6	1.87×10^7

accurate estimation of the circulating pump power inside the resonator [30].

The propagation loss α is estimated using [44]

$$\alpha = \frac{2\pi n_g}{Q_{int}\lambda_0} = \frac{\nu_0}{Q_{int} \cdot R \cdot \mathrm{FSR}}, \tag{3}$$

where n_g is the group index, Q_{int} is the intrinsic quality factor, λ_0 is the resonant wavelength in vacuum, and λ_0 is the corresponding frequency. With a Q_{int} around 17 million, we calculated propagation loss of ~2.1 dB/m, which includes both the scattering loss and material absorption loss. This number is below the estimated material absorption loss of 3.0 dB/m in Ref. [34], and suggests that our Si_3N_4 material has much lower material absorption.

We also characterized the quality factors of the quasi-TM modes of the two resonators. For resonator A, there are three quasi-TM modes with FSRs of 24.3, 24.02, and 23.5 GHz, respectively. We assigned the mode with 24.3 GHz FSR as the fundamental TM mode, which exhibits high Qs. The highest-loaded Q was fitted to be 7.4×10^6, with an on-resonance attenuation of 3.9 dB. Assuming under-coupling condition, we calculated an intrinsic Q of 9.0×10^6. Three TM modes of the same FSRs were observed in resonator B, with similar loaded and intrinsic Qs.

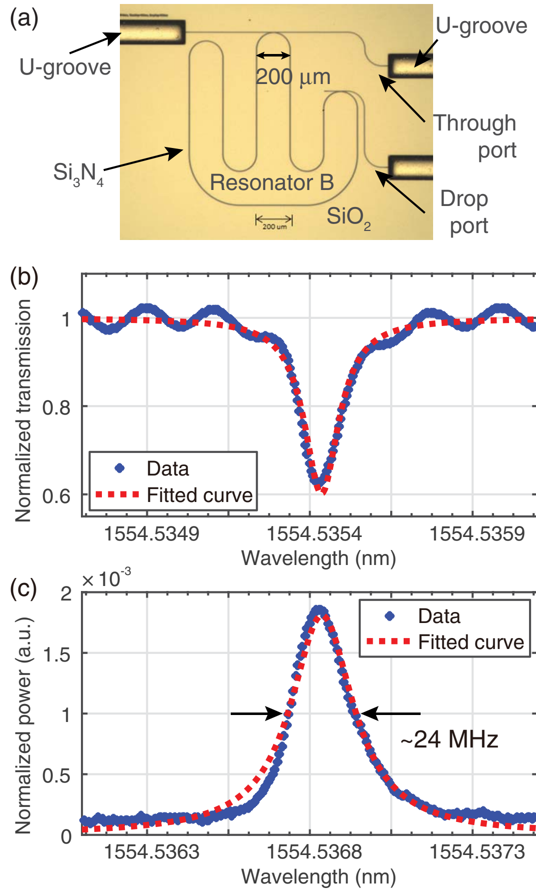

Fig. 9. (a) Optical image showing another "finger-shaped" resonator with both a through port and drop port (hereafter referred to as resonator B). The coupling gap between the through port waveguide and the resonator is 400 nm, and the gap between the drop port waveguide and the resonator is 700 nm. (b) Normalized through port transmission at one resonance. (c) Normalized drop port transmission at the same resonance showing a loaded Q of 8.25 million. The spectra in (b) and (c) were taken in two scans and thus had very slight difference in the resonance wavelength.

4. LOW-THRESHOLD FREQUENCY COMB GENERATION

With a high intrinsic Q of ~17 million, the power requirements for frequency comb generation on a SiN platform can be drastically reduced as the threshold power scales down with Q^2 for Kerr comb generation. All the comb generation results reported here are from quasi-TE modes.

The lowest threshold pump power we observed so far for resonator A is 4.2 mW. Taking into account the 2.5 dB coupling loss per facet, the onset power for first sideband generation should be around 2.36 mW on chip [Fig. 10(a)]. To compare this experimental result with the calculated threshold using Eq. (1), we conducted a number of scans around the resonance, which was around 1564.70 nm, and found that the extracted loaded and intrinsic Qs were stable and had the values of $Q_{\mathrm{loaded}} = 1.16 \times 10^7$ and $Q_{\mathrm{int}} = 1.55 \times 10^7$. With an $A_{\mathrm{eff}} = 1.5\ \mu\mathrm{m}^2$ through mode simulation and $n_2 = 2.4 \times 10^{-19}\ \mathrm{m}^2/\mathrm{W}$ [45], we calculated the threshold power to be 2.2 mW, showing good consistency with the observed threshold power of 2.36 mW.

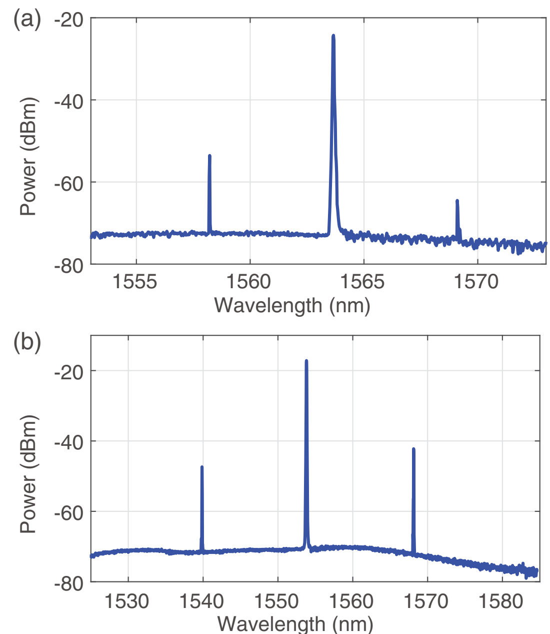

Fig. 10. Low pump power for frequency comb initiation in resonator A. (a) First sideband appears at 2.36 mW on-chip pump power (4.2 mW in fiber), for a resonance at 1564.708 nm. (b) First sideband appears at 2.8 mW on-chip pump power (5.0 mW in fiber), for a resonance at 1553.697 nm.

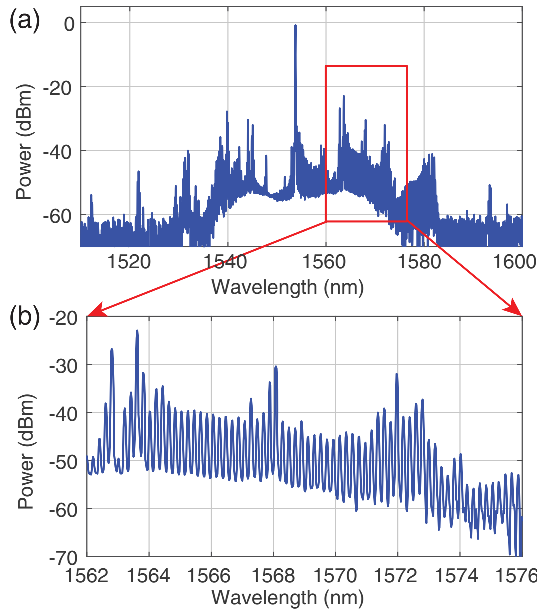

Fig. 11. Single-FSR comb generated in resonator B with a pump power of 24 mW in the bus waveguide (through port).

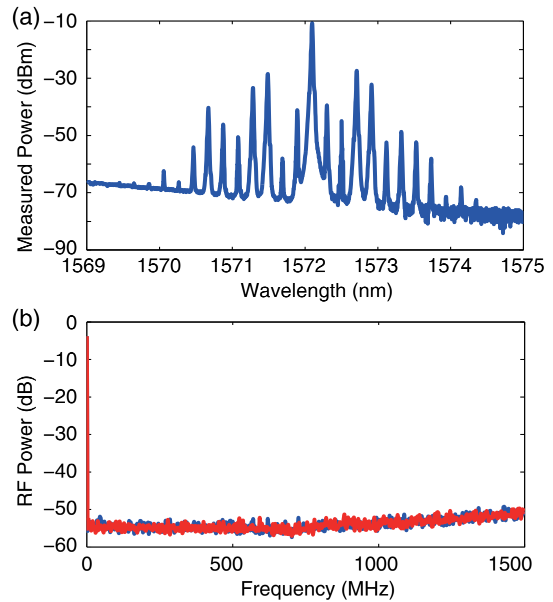

Fig. 12. Low-RF noise, single FSR FC generation in resonator A. (a) Frequency comb spectrum with a low pump power of 27 mW at a resonance of 1571.608 nm. (b) RF spectrum of the recorded FC (in red) and the background (in blue).

We then measured the threshold power at near 1553.696 nm and measured a pump power at 2.8 mW on-chip when the first set of sidebands was observed.

In comparison to the analytical formula of Eq. (1), we found that if we assume the resonance to be under-coupled, a threshold power of 3.8 mW would be required, which is higher than what we observed experimentally. Meanwhile, if we assumed over-coupling, the threshold would come out to be 2.7 mW, almost identical to the experimental observation.

The consistency with threshold power calculations is another evidence of the high Qs we have achieved in Si_3N_4 resonators, as well as the correct mode assignment and identification of coupling regimes.

When pump power increases, more comb lines arise, and Fig. 11 illustrates the generation of one-FSR comb (24.7 GHz) with a number of comb lines at a pump power of 24 mW in resonator B. However, currently such comb lines result in high RF beat noise and thus are not coherent.

Simulation results indicate that a Si_3N_4 waveguide with a cross section of 3 μm × 600 nm has a normal dispersion; it does not change significantly for a broad wavelength range between 1.2 and 1.8 μm, and is −120 ps/nm/km at 1550 nm. An avoided crossing in resonator A can be observed around 1572 nm, which suggests mode interaction between different transverse mode families. Following the pinning of the first sidebands at the mode interaction region as reported in Ref. [21], we pumped resonator A at 1571.69 nm and observed single-FSR FC at a very low pump power of 27 mW [Fig. 12(a)]. The radio-frequency (RF) beating noise of the generated comb is shown in red in Fig. 12(b), which is almost identical to the measurement background, demonstrating low RF noise. The large anomalous group velocity dispersion (GVD) in the mode interaction region suggests that the generated comb is natively mode spaced [46] (or Type 1 [20]) and that should be coherent, even though autocorrelation is not performed due to the comb lines being out of the gain bandwidth of EDFAs. Such low-pump-power combs, despite covering a rather limited frequency band, might be suitable as optical carriers in photonics-assisted RF signal processing where a broad-bandwidth comb is not absolutely needed [13].

5. DISCUSSION AND CONCLUSIONS

In this paper, we described a procedure that has allowed us to fabricate thick Si_3N_4 resonators that achieved very high intrinsic Qs around 17 million while maintaining a small FSR at ~25 GHz. Three methods of characterization, high-resolution tunable laser scanning, cavity ring-down measurement, and onset power for the first sideband, all confirmed the existence of high-Q modes as well as the intrinsic Q values.

Substantial reduction in pump power for frequency comb generation on the Si_3N_4 platform has been achieved. The comb initiation power (or threshold power) of 2.36 mW and low-RF noise, 25 GHz FSR comb generation power at 27 mW are comparable with previous demonstrations of low-threshold-power comb generation with a ridge-shaped SiO_2 resonator having a Q of 2.7×10^8 at 33 GHz FSR [15], or a 13.81 GHz FSR comb generated with a CaF_2 resonator having a Q as high as 6×10^9 [23]. Moreover, such power levels are within the reach of on-chip compound semiconductor lasers.

While we have not reached a fabrication process that can predictably achieve intrinsic Qs larger than 10 million, here we offer a few guidelines that we believe should increase the quality factors.

First of all, the observation that “finger shaped” racetrack resonators, despite having mode-mismatch losses at the junctions between bends and straight sections, exhibit higher Qs suggests two plausible causes. One is that the mode would stay closer to the center of the straight waveguide, which helps to reduce the scattering loss due to sidewall roughness [47] compared to the bend mode, which leans more toward the outer edge of the waveguide. The other is that the EBL would prefer writing straight sections rather than bends, due to the Cartesian configuration

of the beam-deflection mechanism. The EBL will have to fracture the bends and approximate them with polygons, which increases sidewall roughness, so it is advisable to design the resonator to have as much as possible straight segments and minimize the amount of complicated curves. These, together with the requirement of fitting the entire pattern within a write field of the EBL, leads to the "finger-shaped" resonator design in our case. A trade-off is the bending radius versus propagation loss, as too small a radius will lead to high bending loss. In our case, a 100 μm bending radius appears sufficiently large.

Reducing the film thickness will generally increase the Q as the area of waveguide sidewalls, which have roughness caused by etching, will decrease. For Si_3N_4-based resonators, increasing the film thickness beyond 600 nm typically will require an additional cycle of Si_3N_4 deposition, which may incorporate an additional thin layer of SiO_2 or SiON between the Si_3N_4 layers deposited in different cycles. Moreover, thicker films generally have larger top surface roughness and higher probability of particle inclusion. For these reasons, achieving similar levels of Qs in Si_3N_4 resonators with thickness corresponding to anomalous GVD, i.e., 750 nm or larger, is more challenging. However, high intrinsic Q values up to 7×10^6 have been reported [34]. We have achieved, in 100 μm radius rings with 800 nm film thickness, an intrinsic Q of 5.9×10^6 for a ring width of 3 μm and an intrinsic Q of 7.7×10^6 for a ring width of 5 μm.

Increasing the waveguide width will also increase the Q, as the mode will stay further away from the sidewalls as indicated in Refs. [47] and [35], but may cause difficulty in coupling from the bus waveguide to the fundamental mode in the resonator unless a vertical coupling scheme is adopted [35]. For FC generation, a larger waveguide width will increase the effective pump mode area and, according to Eq. (1), will increase the threshold power.

The highest reported intrinsic Qs of Si_3N_4-based resonators are ∼81 million [36]. However, such devices have the majority of optical power residing in the cladding oxide due to the extremely thin waveguide cross section. Consequently, the intrinsic Q is not limited by the material absorption of Si_3N_4. Such resonators are not desirable for FC generation due to the strong GVD as well as the reduction in effective Kerr nonlinearity. It remains interesting, however, to see if the material absorption of Si_3N_4 can be further pushed down by improved film deposition and allow further improvement of Qs in our resonators.

Coupled with the Si_3N_4 platform's material and process compatibility with CMOS foundries, the pump power reduction to the range achievable with on-chip tunable laser sources could lead to monolithically integrated frequency comb sources. High-Q resonators can also find various applications in linear systems. Therefore, our demonstration of high-Q Si_3N_4 resonators may facilitate the development of a variety of novel photonic devices and systems.

Funding. Defense Advanced Research Projects Agency (DARPA) (W31P40-13-1-0018); Air Force Office of Scientific Research (AFOSR) (FA9550-12-1-0236, FA9550-15-1-0211); National Science Foundation (NSF) (ECCS-1509578).

[†]These authors contributed equally to this work.

REFERENCES

1. K. J. Vahala, "Optical microcavities," Nature **424**, 839–846 (2003).
2. L. Fan, J. Wang, L. T. Varghese, H. Shen, B. Niu, Y. Xuan, A. M. Weiner, and M. Qi, "An all-silicon passive optical diode," Science **335**, 447–450 (2012).
3. J. Wang, H. Shen, L. Fan, R. Wu, B. Niu, L. T. Varghese, Y. Xuan, D. E. Leaird, X. Wang, F. Gan, A. M. Weiner, and M. Qi, "Reconfigurable radio-frequency arbitrary waveforms synthesized in a silicon photonic chip," Nat. Commun. **6**, 5957 (2015).
4. P. Ma, D.-Y. Choi, Y. Yu, Z. Yang, K. Vu, T. Nguyen, A. Mitchell, B. Luther-Davies, and S. Madden, "High *Q* factor chalcogenide ring resonators for cavity-enhanced MIR spectroscopic sensing," Opt. Express **23**, 19969–19979 (2015).
5. L. He, S. K. Ozdemir, J. Zhu, W. Kim, and L. Yang, "Detecting single viruses and nanoparticles using whispering gallery microlasers," Nat. Nanotechnol. **6**, 428–432 (2011).
6. A. González Tudela, C. L. Hung, D. E. Chang, J. I. Cirac, and H. J. Kimble, "Subwavelength vacuum lattices and atom-atom interactions in two-dimensional photonic crystals," Nat. Photonics **9**, 320–325 (2015).
7. J. S. Douglas, H. Habibian, C. L. Hung, A. V. Gorshkov, H. J. Kimble, and D. E. Chang, "Quantum many-body models with cold atoms coupled to photonic crystals," Nat. Photonics **9**, 326–331 (2015).
8. M. Aspelmeyer, T. J. Kippenberg, and F. Marquardt, "Cavity optomechanics," Rev. Mod. Phys. **86**, 1391–1452 (2014).
9. P. Del'Haye, A. Schliesser, O. Arcizet, T. Wilken, R. Holzwarth, and T. J. Kippenberg, "Optical frequency comb generation from a monolithic microresonator," Nature **450**, 1214–1217 (2007).
10. T. J. Kippenberg, R. Holzwarth, and S. A. Diddams, "Microresonator-based optical frequency combs," Science **332**, 555–559 (2011).
11. T. Udem, R. Holzwarth, and T. W. Hansch, "Optical frequency metrology," Nature **416**, 233–237 (2002).
12. J. Pfeifle, V. Brasch, M. Lauermann, Y. Yu, D. Wegner, T. Herr, K. Hartinger, P. Schindler, J. Li, D. Hillerkuss, R. Schmogrow, C. Weimann, R. Holzwarth, W. Freude, J. Leuthold, T. J. Kippenberg, and C. Koos, "Coherent terabit communications with microresonator Kerr frequency combs," Nat. Photonics **8**, 375–380 (2014).
13. X. Xue, Y. Xuan, H.-J. Kim, J. Wang, D. E. Leaird, M. Qi, and A. M. Weiner, "Programmable single-bandpass photonic RF filter based on Kerr comb from a microring," J. Lightwave Technol. **32**, 3557–3565 (2014).
14. H. Lee, T. Chen, J. Li, K. Y. Yang, S. Jeon, O. Painter, and K. J. Vahala, "Chemically etched ultra high-*Q* wedge-resonator on a silicon chip," Nat Photonics **6**, 369–373 (2012).
15. J. Li, H. Lee, T. Chen, and K. J. Vahala, "Low-pump-power, low-phase-noise, and microwave to millimeter-wave repetition rate operation in microcombs," Phys. Rev. Lett. **109**, 233901 (2012).
16. L. Razzari, D. Duchesne, M. Ferrera, R. Morandotti, S. T. Chu, B. E. Little, and D. J. Moss, "CMOS-compatible integrated optical hyper-parametric oscillator," Nat. Photonics **4**, 41–45 (2010).
17. S. B. Papp and S. A. Diddams, "Spectral and temporal characterization of a fused-quartz-microresonator optical frequency comb," Phys. Rev. A **84**, 053833 (2011).
18. S. B. Papp, K. Beha, P. Del'Haye, F. Quinlan, H. Lee, K. J. Vahala, and S. A. Diddams, "Microresonator frequency comb optical clock," Optica **1**, 10–14 (2014).
19. J. S. Levy, A. Gondarenko, M. A. Foster, A. C. Turner-Foster, A. L. Gaeta, and M. Lipson, "CMOS-compatible multiple-wavelength oscillator for on-chip optical interconnects," Nat. Photonics **4**, 37–40 (2010).
20. F. Ferdous, H. Miao, D. E. Leaird, K. Srinivasan, J. Wang, L. Chen, L. T. Varghese, and A. M. Weiner, "Spectral line-by-line pulse shaping of on-chip microresonator frequency combs," Nat. Photonics **5**, 770–776 (2011).
21. Y. Liu, Y. Xuan, X. Xue, P.-H. Wang, S. Chen, A. J. Metcalf, J. Wang, D. E. Leaird, M. Qi, and A. M. Weiner, "Investigation of mode coupling in normal-dispersion silicon nitride microresonators for Kerr frequency comb generation," Optica **1**, 137–144 (2014).
22. H. Jung, C. Xiong, K. Y. Fong, X. Zhang, and H. X. Tang, "Optical frequency comb generation from aluminum nitride microring resonator," Opt. Lett. **38**, 2810–2813 (2013).
23. I. S. Grudinin, N. Yu, and L. Maleki, "Generation of optical frequency combs with a CaF_2 resonator," Opt. Lett. **34**, 878–880 (2009).
24. W. Liang, A. A. Savchenkov, A. B. Matsko, V. S. Ilchenko, D. Seidel, and L. Maleki, "Generation of near-infrared frequency combs from a MgF_2 whispering gallery mode resonator," Opt. Lett. **36**, 2290–2292 (2011).

25. T. Herr, V. Brasch, J. D. Jost, C. Y. Wang, N. M. Kondratiev, M. L. Gorodetsky, and T. J. Kippenberg, "Temporal solitons in optical microresonators," Nat. Photonics **8**, 145–152 (2014).
26. V. Brasch, M. Geiselmann, T. Herr, G. Lihachev, M. H. P. Pfeiffer, M. L. Gorodetsky, and T. J. Kippenberg, "Photonic chip-based optical frequency comb using soliton Cherenkov radiation," Science **351**, 357–360 (2016).
27. X. Xue, Y. Xuan, Y. Liu, P.-H. Wang, S. Chen, J. Wang, D. E. Leaird, M. Qi, and A. M. Weiner, "Mode-locked dark pulse Kerr combs in normal-dispersion microresonators," Nat. Photonics **9**, 594–600 (2015).
28. X. Xue, Y. Xuan, P.-H. Wang, Y. Liu, D. E. Leaird, M. Qi, and A. M. Weiner, "Normal-dispersion microcombs enabled by controllable mode interactions," Laser Photon. Rev. **9**, L23–L28 (2015).
29. S. A. Miller, Y. Okawachi, S. Ramelow, K. Luke, A. Dutt, A. Farsi, A. L. Gaeta, and M. Lipson, "Tunable frequency combs based on dual microring resonators," Opt. Express **23**, 21527–21540 (2015).
30. P.-H. Wang, Y. Xuan, L. Fan, L. T. Varghese, J. Wang, Y. Liu, X. Xue, D. E. Leaird, M. Qi, and A. M. Weiner, "Drop-port study of microresonator frequency combs: power transfer, spectra and time-domain characterization," Opt. Express **21**, 22441–22452 (2013).
31. T. J. Kippenberg, S. M. Spillane, and K. J. Vahala, "Kerr-nonlinearity optical parametric oscillation in an ultra high-*Q* toroid microcavity," Phys. Rev. Lett. **93**, 083904 (2004).
32. S. W. Huang, J. Yang, J. Lim, H. Zhou, M. Yu, D. L. Kwong, and C. W. Wong, "A low-phase-noise 18 GHz Kerr frequency microcomb phase-locked over 65 THz," Sci. Rep. **5**, 13355 (2015).
33. M. H. P. Pfeiffer, A. Kordts, V. Brasch, M. Zervas, M. Geiselmann, J. D. Jost, and T. J. Kippenberg, "Photonic Damascene process for integrated high-*Q* microresonator based nonlinear photonics," Optica **3**, 20–25 (2016).
34. K. Luke, A. Dutt, C. B. Poitras, and M. Lipson, "Overcoming Si_3N_4 film stress limitations for high quality factor ring resonators," Opt. Express **21**, 22829–22833 (2013).
35. Q. Li, A. A. Eftekhar, M. Sodagar, Z. Xia, A. H. Atabaki, and A. Adibi, "Vertical integration of high-*Q* silicon nitride microresonators into silicon-on-insulator platform," Opt. Express **21**, 18236–18248 (2013).
36. D. T. Spencer, J. F. Bauters, M. J. R. Heck, and J. E. Bowers, "Integrated waveguide coupled Si_3N_4 resonators in the ultra high-*Q* regime," Optica **1**, 153–157 (2014).
37. K. H. Nam, I. H. Park, and S. H. Ko, "Patterning by controlled cracking," Nature **485**, 221–224 (2012).
38. K. Luke, Y. Okawachi, M. R. E. Lamont, A. L. Gaeta, and M. Lipson, "Broadband mid-infrared frequency comb generation in a Si_3N_4 microresonator," Opt. Lett. **40**, 4823–4826 (2015).
39. O. Schwelb, "Transmission, group delay, and dispersion in single-ring optical resonators and add/drop filters—a tutorial overview," J. Lightwave Technol. **22**, 1380–1394 (2004).
40. P. Del'Haye, O. Arcizet, M. L. Gorodetsky, R. Holzwarth, and T. J. Kippenberg, "Frequency comb assisted diode laser spectroscopy for measurement of microcavity dispersion," Nat. Photonics **3**, 529–533 (2009).
41. D. K. Armani, T. J. Kippenberg, S. M. Spillane, and K. J. Vahala, "Ultra-high-*Q* toroid microcavity on a chip," Nature **421**, 925–928 (2003).
42. B. E. Little, J. P. Laine, and S. T. Chu, "Surface-roughness-induced contradirectional coupling in ring and disk resonators," Opt. Lett. **22**, 4–6 (1997).
43. M. Borselli, T. Johnson, and O. Painter, "Beyond the Rayleigh scattering limit in high-Q silicon microdisks: theory and experiment," Opt. Express **13**, 1515–1530 (2005).
44. P. Rabiei, W. H. Steier, C. Zhang, and L. R. Dalton, "Polymer micro-ring filters and modulators," J. Lightwave Technol. **20**, 1968–1975 (2002).
45. K. Ikeda, R. E. Saperstein, N. Alic, and Y. Fainman, "Thermal and Kerr nonlinear properties of plasma-deposited silicon nitride/silicon dioxide waveguides," Opt. Express **16**, 12987–12994 (2008).
46. T. Herr, K. Hartinger, J. Riemensberger, C. Y. Wang, E. Gavartin, R. Holzwarth, M. L. Gorodetsky, and T. J. Kippenberg, "Universal formation dynamics and noise of Kerr-frequency combs in microresonators," Nat. Photonics **6**, 480–487 (2012).
47. T. J. Kippenberg, J. Kalkman, A. Polman, and K. J. Vahala, "Demonstration of an erbium-doped microdisk laser on a silicon chip," Phys. Rev. A **74**, 051802 (2006).

128.46.71.41 {ts '2017-05-16 10:46:23'}